

Assessing Groundwater Level Change and Aquifer Parameters Across Los Angeles and Orange County Using InSAR Measurements and Machine Learning

Shuaiying Wu^{1b}, Guoxiang Liu^{1b}, Xiaowen Wang^{1b}, *Member, IEEE*, Hongguo Jia^{1b}, Yihang Ding, Bo Zhang^{1b}, and Wenfei Mao^{1b}, *Member, IEEE*

Abstract—Combining observation well data and Interferometric Synthetic Aperture Radar (InSAR) deformation has shown great promise in groundwater levels monitoring and aquifer parameters estimation, which is crucial for groundwater management and related natural hazards anticipating. However, insufficient observation wells bring a drawback of this means in obtaining high spatial resolution results. Here, we employ a machine learning approach, the optimizable Gaussian regression learner, to integrate these two datasets to derive pixel-scale groundwater levels across Los Angeles and Orange County from Jun. 2015 to Nov. 2021. The results are validated with groundwater levels revealed from relative changes in seismic velocity (dv/v) measured at a dense network. With the innovative results, we found an interesting phenomenon that the groundwater levels show an overall rising trend during the study period, which is prominent in the San Gabriel Valley and the Coastal Plain of Orange County (CPOC) basins with mean rate of 0.78 ± 0.04 and 0.31 ± 0.05 m/yr, respectively. Besides, the strongest seasonal groundwater level changes are observed in the CPOC with mean annual amplitude of 0.97 ± 0.16 mm, which results in seasonal ground deformation for 3.58 ± 0.51 mm. Moreover, by analyzing the long-term hydraulic head records in these two basins, we identify that the rising trends should be attributed to ~ 6.5 -year interannual variations. Our study underlines the importance of integrating multitemporal InSAR data with hydraulic head measurements to accurately quantify changes in groundwater levels, determine aquifer parameters, and assess variations in groundwater storage.

Index Terms—Aquifer parameters, groundwater, interferometric synthetic aperture radar (InSAR), machine learning, multitemporal analysis.

Received 8 January 2025; revised 11 March 2025 and 10 April 2025; accepted 1 May 2025. Date of publication 7 May 2025; date of current version 22 May 2025. This work was supported by the National Natural Science Foundation of China under Grant 42171355 and Grant 42401535. (*Corresponding authors: Guoxiang Liu; Xiaowen Wang.*)

Shuaiying Wu, Guoxiang Liu, Xiaowen Wang, Hongguo Jia, and Wenfei Mao are with the Faculty of Geosciences and Environmental Engineering, Southwest Jiaotong University, Chengdu 611756, China (e-mail: shining@my.swjtu.edu.cn; rsgxliu@swjtu.edu.cn; insarwxw@swjtu.edu.cn; rsjia@swjtu.edu.cn; wenfei192912@163.com).

Yihang Ding is with the Department of Hydraulic Engineering, Tsinghua University, Beijing 100084, China (e-mail: yhdng@tsinghua.edu.cn).

Bo Zhang is with the Institute of Mountain Hazards and Environment, Chinese Academy of Sciences, Chengdu 610299, China (e-mail: rsbozh@imde.ac.cn).

This article has supplementary downloadable material available at <https://doi.org/10.1109/JSTARS.2025.3567660>, provided by the authors.

Digital Object Identifier 10.1109/JSTARS.2025.3567660

I. INTRODUCTION

GROUNDWATER constitutes approximately 30% of global freshwater and serves as the primary water source for domestic consumption, industrial development, and irrigation. In recent decades, the global increase in population and urbanization has intensified the demand for water resources, causing excessive extraction of groundwater from numerous aquifers around the world [1], [2], [3], [4], [5]. Over-exploitation of ground-water can lead to a decline in the water table, diminished surface water availability, and an elevated risk of seawater intrusion in coastal regions. As a result, the monitoring of changes in groundwater levels holds immense significance. This practice is vital for assessing the condition of aquifer systems and variations in groundwater storage (GWS), which in turn enhances our understanding of hydrological processes and supports the sustainable management of freshwater resources.

The measurement of hydraulic head changes in wells has been extensively employed in groundwater management. Nonetheless, due to limited coverage and high operational costs, this approach is mainly suited for small-scale studies [6]. Changes in aquifer recharge and drainage can lead to variations in properties such as pore pressure, saturation, porosity, and microstructures within water-saturated rock formations, which can be recorded by the relative changes in seismic velocity (dv/v). Utilizing the dv/v method has emerged as an alternative approach to infer modifications in groundwater levels [7], [8]. However, same as monitoring wells, this technique has a drawback of low spatial coverage. Besides, since any changes in underground medium would result in disturbances in dv/v , it is needed to validate by monitoring well observations.

The utilization of advanced gravimetric satellites, like the gravity recovery and climate experiment (GRACE) and its successor, GRACE Follow-On (GRACE/FO), has revolutionized the assessment of variations in GWS on continental and basin scales [9], [10], [11]. Nevertheless, the GRACE/FO system is characterized by a coarse spatiotemporal resolution (350×350 km and a monthly basis) and necessitates additional data to separate GWS changes [12] from the inferred fluctuations in terrestrial water storage. Contemporary hydro-logical models, such as the WaterGAP Global Hydrology Model, PCRaster Global Water Balance, and Global Land Data Assimilation System Catchment Land Surface Model (GLDAS CLSM), directly

supply GWS data. However, these models frequently lack specific information about aquifer depth and tend to underestimate the actual GWS volume [13].

In recent years, the inversion of ground surface deformation and hydraulic head data using a compaction model of aquifer systems has emerged as a powerful method for constraining GWS changes and aquifer properties [14], [15]. Specifically, Interferometric Synthetic Aperture Radar (InSAR) deformation have been proven valuable in estimating hydrological parameters and groundwater storage changes, which complements data sources aforementioned with exceptional spatiotemporal resolution. Based on InSAR and hydraulic head data, Neely et al. [6] discovered a substantial subsidence in the San Joaquin Valley during 2016, which was linked to escalated groundwater pumping; Zhu et al. [16] revealed a seasonal fluctuation in groundwater levels of 16.6 m between 2015 and 2018 in the Santa Ana basin, leading to a seasonal ground uplift of 9.8 mm; Jiang et al. [4] identified the irrecoverable GWS change accounted for more than 96% of the total GWS depletion in North China Plain. Other notable findings have also been made in such as the Madrid aquifer in Spain, Southern California in the United States, and Central Mexico [1], [3], [5], [17].

However, obtaining high spatial resolution groundwater level changes by integrating InSAR and hydraulic head data is challenging due to the sparse coverage of the observation well. The successful integration of InSAR measurements and in situ hydraulic head data requires the accurate interpolation of sparse head data to align with the spatial resolution of InSAR. An interpolation method that is both dependable and precise is imperative that any inadequacy in this regard can potentially introduce significant uncertainties into the interpretation of aquifer systems and groundwater storage dynamics [2], [36]. To enhance the combination of these two data for the study of aquifer systems, ML-based approaches have been introduced to address the limitations inherent in conventional interpolation methods [37], [38], [39], [40], [41]. In comparison to traditional interpolation techniques, such as Kriging and inverse distance weighted (IDW) interpolations, ML-based methods allow for the inclusion of high-spatiotemporal InSAR measurements, geological settings, and climate factors as inputs, ensuring more reliable interpolation [39], [41]. With the application of ML methods, Wang et al. [42] found that the land subsidence in Decheng county, Shandong Province in China should be mainly attributed to groundwater level changes; Naghibi et al. [43] successfully acquired continuous ground deformation map from the discrete InSAR measurement due to vegetation decorrelation in the farming area; Wang et al. [44] first identified the feasibility of assessing the risk of land subsidence in Yellow River Delta with InSAR ground deformation data only.

In south California, except for the impact of human activities, more frequent extreme climate and weather events, like droughts and floods, aggregate the uncertainties in groundwater variabilities. Thus, an in-depth and accurate analysis of groundwater levels at difference time scales is necessary. Here, we use a robust ML-based approach, the optimizable Gaussian process regression (OGPR) learner [18], to integrate InSAR and hydraulic head data for obtaining pixel-scale groundwater level changes.

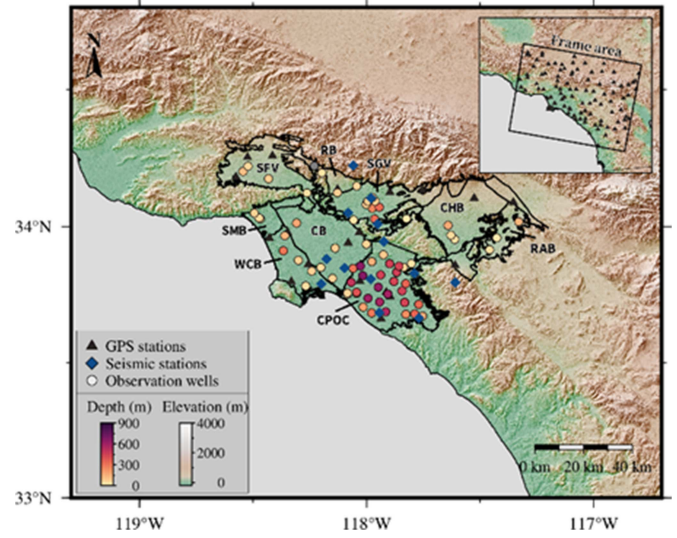


Fig. 1. Geolocation of the study area, with the black triangles, dark blue diamonds, and colored circles represent the GNSS stations, seismic stations, and observation wells, respectively. Black triangles in the subplot represent GNSS stations used for InSAR calibration and validation. Depth of observation well means depth to land surface. SGV: San Gabriel Valley; CPOC: Coastal Plain of Orange County; SFV: San Fernando Valley; CHB: Chino Basin; CB: Central Basin; WCB: West Coast Basin.

To streamline the ML training process and alleviate overfitting concerns, we analyzed the spatiotemporal patterns of InSAR and head data through blind source separation methods. The obtained results are subsequently compared and validated using outputs from hydrological models, climate factors, and dv/v. Our findings underscore the significance of considering both the spatial and temporal components of deformation and hydraulic head data. This comprehensive approach leads to an improved understanding of the underlying hydrological phenomena.

II. STUDY AREA AND DATA

A. Study Area

The study area is located in south California, encompassing Los Angeles and Orange County (see Fig. 1). It is bordered by mountains and adjacent to the Pacific Ocean in the west. These mountains enclose several groundwater basins, such as the SGV, CPOC, central basin (CB), and San Fernando Valley (SFV). Rivers and streams are interspersed among these basins, with many being redirected to groundwater recharge facilities, particularly in the SGV and San Bernardino. Categorized as Mediterranean climate, the study area exhibits dry summers and rainy winters. Annual precipitation ranges from 250 to 1200 mm across this region and is most prominent in mountainous areas. The major sources of groundwater supply are artificial recharge and winter precipitation. Consequently, groundwater constitutes the primary contributor to total water consumption, accounting for over 40% and 70% of water demand in the Los Angeles and Santa Ana Basin, respectively [16], [19]. As industrialization and urban development have progressed, the increased water demand has led to the excessive groundwater exploitation, which has induced inelastic land subsidence, raising concerns about

the hydrological cycle within the study area. Thus, it is imperative to investigate the spatiotemporal evolution of groundwater variations for effective groundwater management and to characterize hydro-meteorological hazards in Los Angeles and Orange County.

B. Study Data

1) *Hydraulic Head Data*: Hydraulic head data spanning from 2015 to 2022 at 79 observation wells from the California Department of Water Resources (<https://wdl.water.ca.gov/>) were used. For convenience, the continuously observed depth to water surface data was converted to water surface elevation anomaly (hydraulic head). Most observation wells have depths below 100 m (shallow aquifer), except 12 observation wells located in the CPOC, which have a mean depth of 430 m (deep aquifer). Examples of observed hydraulic heads are shown in Fig. S1.

2) *SAR Data*: A total of 175 Sentinel-1 SAR images in descending mode along track 71 are used to map ground deformation in the study area between Jun. 2015 and Nov. 2021. We utilize the commercial GAMMA software to generate SAR interferograms, setting the spatial and temporal baseline thresholds at 200 m and 60 days, respectively. Interferograms with coherence lower than 0.4 are removed, leaving 465 interferograms for time series analysis. As ground deformation in response to groundwater level change predominantly occurs in the vertical direction, we convert that from line-of-sight to vertical, assuming the horizontal displacements are negligible [20]. Note that the reference point is at GNSS site GVR5 located between the CB and SGV basin, where the surface deformation was relatively stable during the study period.

The accuracy of InSAR is significantly affected by atmospheric errors, especially the tropospheric delay for C-band satellites, which can reach up to several tens of meters within individual interferograms [21], [22]. In this study, we rectify the tropospheric delays in each interferogram using the Generic Atmospheric Correction Online Service product [23]. To further address the long-wavelength error resulting by unmodeled atmospheric delay, we follow Neely et al. [24] and apply the GInSAR method by adding a surface that fits the differences between InSAR- and GNSS-vertical displacements. The vertical displacement time series (VDTs) are then retrieved with the Small Baseline Subset approach. The detailed processing is provided in Text T1. The great agreement (mean CC of 0.67 and mean root-mean-square error (RMSE) of 3.5 mm) between InSAR- and GNSS- VDTs at twelve typical GNSS stations identify the feasibility of our processing strategy (Fig. S2).

3) *Seismic Ambient Noise Data*: We use the continuous records of vertical component ambient seismic noise at 11 broadband seismic stations in the California Integrated Seismic Network from Jan. 2015 to Dec. 2021. To acquire the noise cross-correlation functions (CCFs), the daily noise records are preprocessed by [7], [25], [26]: 1) applying the instrument correction; 2) removing the mean and trend, and downsampling to 20 Hz; 3) whitening over 0.5–2.0 Hz in frequency domain and 1-bit normalization in time domain. The CCFs are computed

between station pairs within 50 km every hour, with 30 min of overlap between successive hours. The hourly CCFs are stacked to form daily CCFs, and the reference CCFs are derived by stacking all daily CCFs.

The Moving Window Cross-Spectrum technique is then applied to obtain daily relative changes in seismic velocity (dv/v) [25]. First, we compute the time delay (dt) between the daily- and reference- CCFs along causal and acausal parts of the coda (10 s window and 2 s shifting in the SGV; 20 s window and 5 s shifting in the CPOC). Then, the daily relative time delay (dt/t) is estimated by a weighted linear regression of all dt per day. Finally, the daily dv/v is equal to $-dt/t$ based on the assumption that dv/v is homogeneous [8].

4) *Auxiliary Data*: GNSS vertical coordinate time series are provided by the Nevada Geodetic Laboratory (<http://geodesy.unr.edu/>), which aims to reduce unmodeled atmospheric error in SAR images and validate our InSAR VDTs. A total of 98 GNSS stations situated within the frame area are selected (black triangles in the subplot of Fig. 1). The daily GNSS data is smoothed by a moving average method with a window of 12 days and resampled in corresponding with SAR acquisition time. The GNSS stations used for InSAR validation are evenly distributed across the study area.

The GWS changes from GLDAS CLSM L4 and modeled from North American Land Data Assimilation System (NLDAS), respectively, are employed to compare and evaluate the GWS change from the ML-based method [27]. NLDAS GWS change is derived by subtracting the surface water storage (the sum of soil moisture and plant canopy water) from the total water storage (the sum of precipitation, evapotranspiration, and runoff). Besides, precipitation, evapotranspiration, and runoff data from NLDAS were also used to investigate the intrinsic driver of groundwater level and GWS change [28].

III. METHODOLOGY

A. Blind Source Separation

Both surface deformation and hydraulic head data encompass components with varying timescales, which include long-term, annual, semiannual, and interannual signals [5]. Consequently, the unprocessed data are insufficient to provide a direct portrayal of the evolving characteristics of confined aquifer properties. An effective strategy involves decomposing the signals of ground deformation and groundwater levels across both time and space, enabling a practical means of discerning the extent to which diverse factors contribute to these changes.

We employ ICA to separate the long-term trends and seasonal components in InSAR VDTs. ICA is a blind source separation method that can identify underlying sources in a dataset. Here, we utilize the FastICA algorithm [29] due to its rapid convergence and stability in decomposition [30]. We follow Ebmeier (2016) to determine the suitable number of ICs by implementing the principal component analysis method and the order of ICs by calculating the importance of each IC to the original deformations. Four ICs (Fig. S3a-d) of the surface deformation with a variance reduction of up to $\sim 90\%$ are considered. In terms of the spatiotemporal variability of each IC, we designate IC1

as the long-term change of surface deformation and the sum of IC2~4 as the seasonal term, respectively.

VMD technique is used to investigate the seasonal fluctuations at each observation well [32]. VMD is an adaptive data analysis technique similar to ICA but better suited for examining the multitemporal characteristics of a single signal [33]. Comparing to EMD, VMD exhibits excellent resistance against mode mixing among the decomposed intrinsic mode functions (IMFs). This resilience enables more robust identification of seasonal patterns [34], [35]. In this study, we first estimate the long-term trends through linear regression before applying VMD to the detrended hydraulic head data. The decomposed results in the SGV and CPOC, as shown in Fig. S4 and S5, demonstrating similar multitemporal patterns within each basin. Here, the IMFs exhibiting a distinct spectrum of approximately 1 cycle per year (cpy) and those below 1 cpy are identified as the annual and interannual signals (Fig. S6) that the sum is considered to represent the seasonal hydraulic heads.

B. Machine Learning Approach

Here, we employ the OGPR to establish a model connecting hydraulic head data with InSAR VDTs. OGPR is a nonparameter and supervised machine learning approach, which aims to learn a function to project the input datasets to the target variable [45]. It seeks to enhance prediction accuracy by optimizing the hyperparameters of GPR through gradient-based methods. Previous studies have demonstrated that OGPR can yield the most accurate predictions compared to traditional regression learning techniques, such as linear regression, support vector machines, and ensembles of trees (Tab. 1) [45], [46], [47]. Specific information for OGPR is in Text T2.

The training dataset for the OGPR comprises predictor and response variables collected from observation wells. The predictors include location coordinates (longitude and latitude), multitemporal VDTs, hydrological factors (precipitation, runoff, and evapotranspiration), and geospatial information (slope, aspect, and elevation), while the response variable is hydraulic heads, which share the same temporal resolution as ground deformation. We used 5-fold method to conduct the ML training process. Specifically steps are: 1) split the dataset divided into 5 subsets randomly, 2) take the subset as a hold out or test data set and take the remaining 4 subsets as a training data set, 3) fit a model on the training set and evaluate it on the test set, 4) repeat steps 2 to 3 for five times and ensure that each subset is used as a test set once. The optimal model is selected based on the lowest RMSE. Subsequently, the trained model is utilized to estimate long-term and seasonal hydraulic head changes for each InSAR pixel, respectively. It is crucial to note that the predictors above must be resampled to match the spatiotemporal resolution of InSAR observations [48].

The optimizing processes of OGPR for long-term and seasonal groundwater levels are shown in Fig. 2(a) and (b), which seek to minimize the model MSE by choosing different values for the hyperparameters, including Basis Function, Covariance Function, Sigma (σ^2, σ_f^2), and Kernel Scale (l). The optimized hyperparameters were both determined after eight iterations with Bayesian optimization. Note that there should be 175 sets

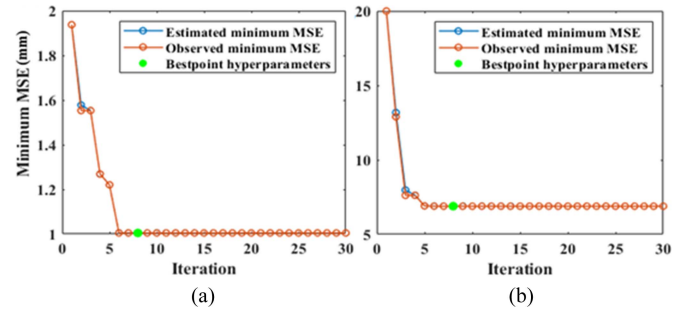


Fig. 2. MSE changes in OGPR iterative process for long-term (a) and seasonal (b) groundwater levels.

of hyperparameters for seasonal groundwater level predictions. But for convenience, hyperparameters for predictions of annual amplitudes were used here, which is reasonable because the annual signal is one of the most prominent components for seasonal surface deformation and hydraulic head data across the study area [5], [49]. In addition, it is worth pointing out that all well data are employed for the training of long-term hydraulic heads, but only 36 well data (deep wells, marked with circles in Fig. 4(a) that are highly consistent with surface deformation are retained for the training of seasonal hydraulic heads.

C. Aquifer Parameters Estimation

Storativity (S) is the most crucial parameter for characterizing an aquifer system's response to hydraulic head changes. It is defined as the volume of water released per unit decline in hydraulic head per unit area of the aquifer system [4]. Assuming water compression is negligible, the storage coefficient (S_k) for confined aquifer can be expressed as follows [50]:

$$S_k = \frac{\Delta b}{\Delta h} \quad (1)$$

where Δb is the confined aquifer compaction approximately equivalent to InSAR deformation, and Δh is hydraulic head change reflecting the change in effective stress.

The S_k consists of elastic (S_{ke}) and inelastic (S_{kv}) skeletal storativity, which are defined based on whether the effective stress σ' exceeds the preconsolidation stress σ'_{\max} [5]

$$S_k = \begin{cases} S_{ke} & \text{for } \sigma' < \sigma'_{\max} \\ S_{kv} & \text{for } \sigma' > \sigma'_{\max} \end{cases} \quad (2)$$

Specifically, the S_{ke} and S_{kv} can be estimated by [50], [51]

$$S_{ke} = \frac{\Delta b_e}{\Delta h_e} \quad \frac{\Delta b_i}{\Delta h_i} = S_{kv} \left(1 - \frac{8}{\pi^2} \right) e^{-\frac{\pi^2 t}{4\tau}}, \Delta b_i = \Delta b - S_{ke} \Delta h \quad (3)$$

where Δb_e and Δh_e represent the elastic surface deformation and seasonal hydraulic head change, while Δb_i and Δh_i are the inelastic surface deformation and long-term hydraulic head change, respectively. Besides, τ is the compaction time constant, and t is the time after the change in head.

After calculating S_{ke} and S_{kv} , the GWS change in confined aquifer can be estimated, consisting of recoverable and

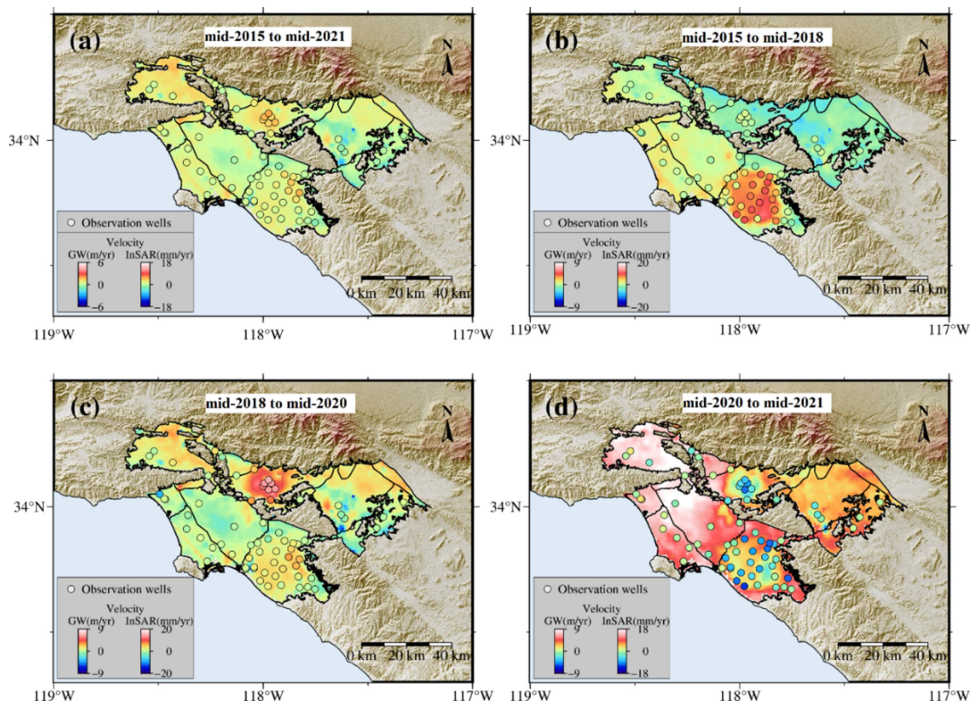


Fig. 3. Velocity maps of IC1 and hydraulic head data during four periods. (a) Mid-2015 to mid-2021. (b) Mid-2015 to mid-2018. (c) Mid-2018 to mid-2020. (d) Mid-2020 to mid-2021.

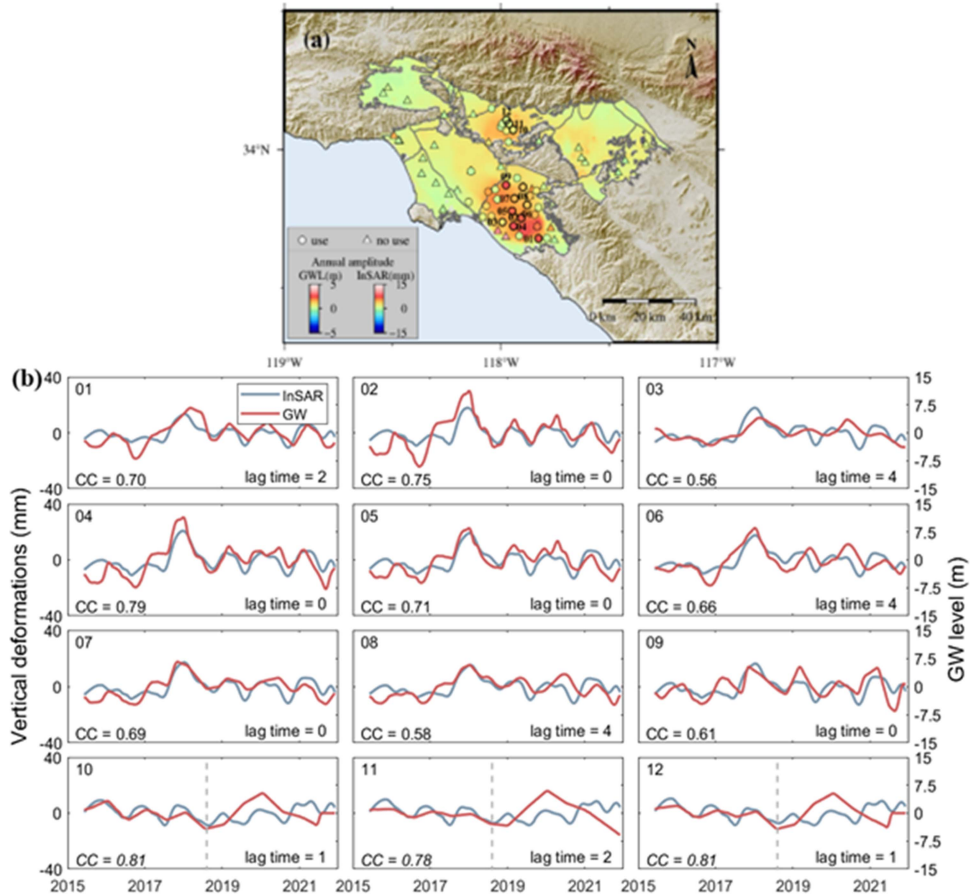


Fig. 4. (a) Annual amplitudes of seasonal surface deformation and hydraulic head change. Circles (high CC), bolded circles (example), and triangles (low CC) represent the observation wells. (b) Comparison of seasonal time series at 12 example wells.

irretrievable components corresponding to the elastic and inelastic compaction, respectively. Here, we use the seasonal InSAR VDTs to estimate the recoverable GWS (RGWS) change $V_r = S_{ke} \times \Delta h_{\text{total}} \times \text{Area}$, where's Δh_{total} is the total hydraulic head change. Moreover, the irretrievable GWS (IGWS) is calculated by $V_i = S_{kv} \times \Delta h_{\text{total}} \times \text{Area}$ [52].

IV. RESULTS

A. Spatiotemporal Patterns of Surface Deformation and Hydraulic Head

1) *Long-Term Variations*: We investigate the multitemporal characteristics of surface deformation across the study area by applying ICA, which provides important insights for understanding the temporal evolution of groundwater change. First, we present a correlation analysis on trends of raw InSAR VDTs and IC1 to assess the ability of ICA to quantify the long-term variations. The results reveal that IC1 has a greater trend than raw InSAR VDTs (Fig. S7). Especially in the northern basins, such as the SFV, SGV, CHB, and RAB, the discrepancies between these two estimates exceeds 1.5 mm/yr. Besides, IC1-based trends demonstrate a stronger correlation with hydraulic heads than raw InSAR VDTs (CC of 0.58 and 0.48, respectively). The results underline that IC1 trend estimates are more capable of surface deformation quantification due to ground-water change.

Especially in the SGV and central CPOC [see Fig. 3(a) and (b)], the long-term changes of ground deformation (IC1) and hydraulic heads show an overall rising trend. The strong correlation indicates that long-term surface deformation is mostly attributed to the land rebound due to the water level recovery. Specifically, land uplift reveals an average rate of 1.32 ± 0.06 mm/yr, which is significant in the SFV (2.80 ± 0.09 mm/yr) and SGV (1.82 ± 0.07 mm/yr) (Tab. 2). The land subsidence is mostly observed in the central CB, north CPOC, and south CHB, whereas the severest subsidence (-13.3 ± 0.41 mm/yr) is found in the south close to the Santa Ana River; the mean rising rate of heads is 0.46 ± 0.08 m/yr, which are prominent in the SGV and the center of CPOC with average values of 1.15 ± 0.09 and 0.55 ± 0.10 m/yr, respectively.

We conducted a more in-depth analysis of velocity maps for surface deformation and hydraulic head values over three periods to enhance our understanding of the variations in aquifer system characteristics. As shown in Fig. 3(b)–(d), surface deformation and hydraulic heads illustrate consistent spatial trends during the first two phases (mid-2015 to mid-2018 and mid-2018 to mid-2020); however, they deviate in the third phase (mid-2020 to mid-2021). These discrepancies suggest that surface deformation, stemming from changes in hydraulic head, predominantly transpired between mid-2015 and mid-2020. Specifically, during the first period, surface deformation displayed a downward trend in the northeast, progressively increasing towards the southwest and peaking in the CPOC with an average rate of 3.94 ± 0.51 mm/yr. Correspondingly, hydraulic head values showcased a similar pattern of change, with the most substantial rise occurring in the same region (mean rate of 2.39 ± 0.22 m/yr). In the second phase, both data observed the highest mean rates for 5.29 ± 0.33 mm/yr and 4.92 ± 0.26 m/yr in the SGV, respectively. While in the third phase, surface deformation

and hydraulic heads demonstrated an overall contrasting trends across the entire study area.

2) *Seasonal Variations*: The seasonal ground deformation serves as a crucial indicator for assessing the seasonal fluctuations in groundwater levels [4], [51]. Here, we investigate the annual amplitudes of seasonal surface deformation to gain our knowledge of the spatial characteristic of seasonal groundwater changes [49]. The annual amplitudes of surface deformation span from approximately 0 to 8.18 ± 0.98 mm, with a mean value of 2.2 ± 0.44 mm. Notably, the SGV and CPOC regions exhibit the most significant amplitudes, measuring 3.14 ± 0.45 mm and 3.58 ± 0.51 mm, respectively, in contrast to other areas where the average amplitude stands at 1.65 ± 0.41 mm. As depicted in Fig. 4, the distribution of annual hydraulic heads matches the spatial pattern observed in surface deformations, particularly noticeable within the SGV and CPOC regions. In the SGV and CPOC basins, hydraulic head values showcase annual fluctuations with mean values of 0.48 ± 0.12 m and 1.33 ± 0.25 m, respectively (details are in Tab. 2).

We extended our investigation by comparing the seasonal time series to assess the connection between surface deformation and hydraulic head variations. Tab. 1 reveals that the highest average cross-correlation (CC) value between these two datasets occurs in the CPOC region (> 0.65) [5]. Within the SGV, these two datasets exhibit significant correlations with an average CC value of up to 0.8 until Aug. 2018. Subsequently, the mean CC drops to less than 0.1 due to the diminished seasonal signals in hydraulic head variations. Conversely, for the remaining basins, the relationship is weak, particularly in the SFV and CHB regions where the average CC remains below 0.1. From the above observations, it can be inferred that seasonality plays a pivotal role in the context of surface deformation in relation to the local groundwater system within Los Angeles and Orange County, primarily concentrated in the SGV and CPOC regions. Fig. 4(b) provides a comparison of seasonal surface deformation and hydraulic head values across 12 representative wells (the comparison of raw InSAR VDTs and hydraulic heads is detailed in Fig. S8).

B. Spatiotemporal Patterns of ML-Predicted Hydraulic Heads and dv/v

1) *Spatial Patterns*: Based on the good agreement between surface deformation and hydraulic heads both at the long-term and seasonal time scales, we utilized a ML approach, the OGPR method, to predict changes in groundwater level at InSAR pixels to evaluate the conditions of aquifer systems and fluctuations in regional groundwater level. The comparison between observed and predicted groundwater levels (depicted in Fig. S9) demonstrates significant agreement, underlining the strong performance and reliability of the OGPR trained model. Particularly, these two data reveal a CC of 0.91 for the trends and a mean RMSE of less than 1.74 mm for the seasonal components, respectively.

As shown in Fig. 5(a), the predicted long-term groundwater levels manifest an overall rising trends and the most significant rates are found in the SGV and CPOC regions with mean of 0.78 ± 0.04 and 0.31 ± 0.05 m/yr, respectively (details

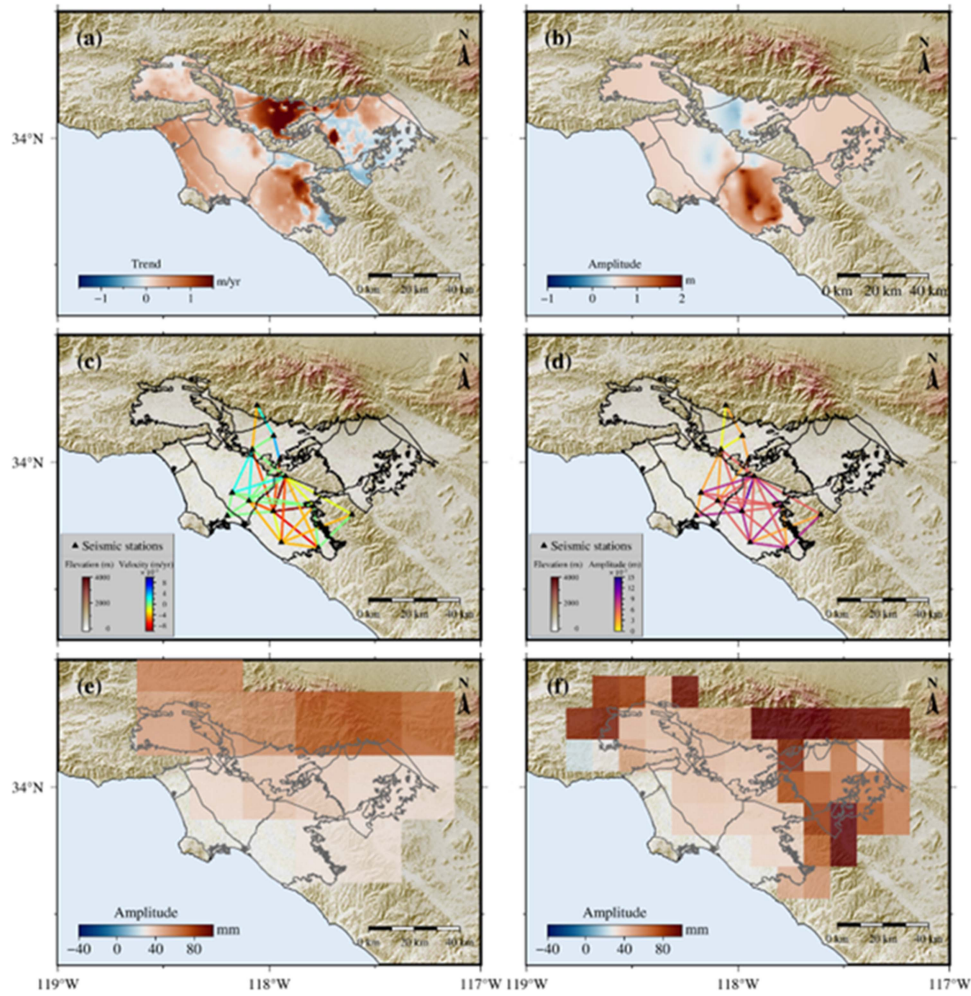


Fig. 5. (a) Predicted long-term hydraulic head change, (b) the annual amplitude for predicted seasonal hydraulic head change, (c) long-term trend, and (d) annual amplitude of dv/v , annual amplitudes of GWS from (e) GLDAS CLSM and (f) NLDAS.

are in Tab. 3). This finding suggests that the primary driver behind long-term surface deformation across the study area is the groundwater level changes, particularly the SGV and CPOC areas. The map of annual amplitudes from predicted seasonal hydraulic heads [see Fig. 5(b)] demonstrate that the notable seasonal fluctuations of groundwater level mainly occurred in the CPOC, which has a mean annual amplitude of 0.97 ± 0.16 m approximately twice as large as the those observed in the other areas (0.54 ± 0.10 m).

Groundwater level affects the medium in subsurface, resulting in changes in the speed of coda wave and dv/v . A rising groundwater level accelerates the speed of coda wave and leads to high dv/v , on the contrary, a decreasing groundwater level reduces the speed of seismic wave and causes low dv/v . Thus, it is feasible to validate the predicted hydraulic heads using dv/v from a dense network. Here, we focus on the frequency range of 0.5 to 2.0 Hz, which exhibits heightened sensitivity to groundwater variations within the upper 500 m of the aquifer. This frequency range is the most promising for groundwater monitoring in most study regions [5], [7]. As shown in Fig. 5(c) and (d), the dv/v estimates display consistent spatial pattern with the predicted hydraulic heads. Obviously, the dv/v have

the propagation path through the CPOC illustrate both notable rising rate and annual amplitude, which provides critical clues for validating ML-predicted hydraulic heads.

We further compare the ML results with model outputs from GLDAS CLSM and NLDAS. Conversely, the model predictions [see Fig. 5(e) and (f)] exhibit smaller amplitudes within the CPOC region but noteworthy values in the northern basin (GLDAS CLSM) and the northeastern basin (NLDAS). Note that the model outputs possess incomplete coverage in the coastal CPOC area due to the relatively low spatial resolutions of GLDAS CLSM ($0.25^\circ \times 0.25^\circ$) and NLDAS ($0.125^\circ \times 0.125^\circ$). Given the strong consistency between the predicted- and observed-hydraulic head data, which are closely linked to changes in GWS, it can be inferred that the model outputs might contain uncertainties when it comes to estimating groundwater changes in coastal aquifers.

2) Temporal Patterns: The most notable groundwater changes within the study area occur in the SGV and CPOC basins [5], [7]. Thus, we examine the average monthly hydraulic heads in these two basins and a neighbor region (CB) to characterize the hydrological dynamics across the study region. As shown in Fig. 6(a)–(c), all monthly groundwater level changes peaked

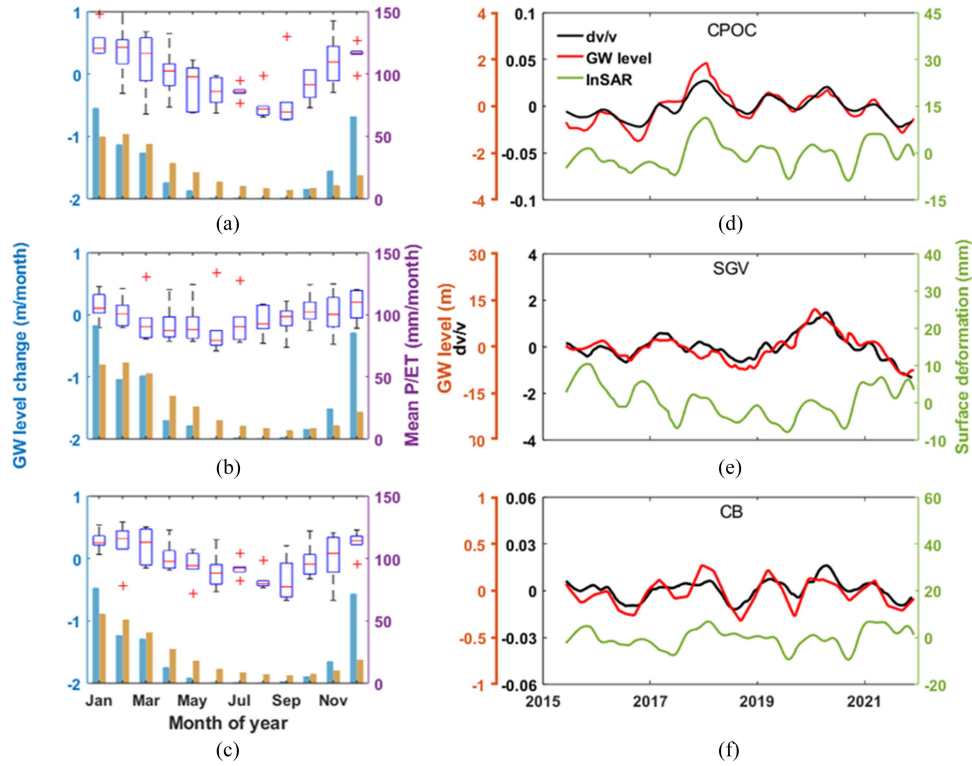


Fig. 6. In the SGV and CPOC, (a)–(c) monthly variations of seasonal hydraulic head changes (box plot), precipitation (blue bar), and the sum of evapotranspiration and runoff (yellow bar), (d)–(f) the comparison of seasonal surface deformation, hydraulic head change, and dv/v .

around January, a trend that aligns with both precipitation variations and the combined effects of runoff and evapotranspiration. This correspondence implies that the vigorous seasonal aquifer recharge in these three regions is heavily influenced by the substantial winter precipitation [5], [15]. Furthermore, within the SGV, a moderate monthly variation is observed, while the most rapid decline in hydraulic head is recorded in May. In contrast, the CPOC and CB experience the swiftest changes in August due to pronounced groundwater withdrawal during the summertime [5].

The good agreement between predicted hydraulic heads and dv/v (mean CC of 0.86) illustrates the promise of leveraging the ML approach applied to InSAR data for tracking groundwater levels. This method has an advantage of being appropriate for both confined and unconfined aquifers, and thus, can be applied to investigate the aquifer properties. We compare the time series of predicted groundwater level and surface deformation to characterize the groundwater cycle and aquifer properties. In the CPOC [see Fig. 6(d)], a synchronous pattern is observed between seasonal changes in these two data sets with a CC of up to 0.74. This coherence indicates the aquifer is confined and the predominant cause of elastic surface deformation in the CPOC can be largely attributed to fluctuations in the seasonal groundwater level. The annual amplitudes of these two data sets are 3.45 ± 0.2 m and 1.1 ± 0.18 mm, respectively. Besides, surface deformation uplifted by 24 mm from the early 2017 to 2018, which was about two times greater than the annual amplitude; concurrently, the groundwater level rose by about 8 m.

In the SGV, the seasonal characteristics are more prominently reflected in the surface deformations compared to the hydraulic head data [see Fig. 6(e)], which results in low relevance (CC of ~ 0.1) between these two datasets and denotes the aquifer is unconfined or semiconfined. Both surface deformations and hydraulic heads revealed decreasing trend during mid-2015 to early 2019 with rates of -3.27 ± 0.16 mm/yr and -1.50 ± 0.19 m/yr, respectively. Subsequently, there was a significant rise in water levels at a rate of 11.71 ± 0.48 m/year from 2019 to 2020, followed by a return to baseline levels until 2022. However, the surface deformation displayed a consistent uplift trend, with a sustained rate of 2.71 ± 0.67 mm/year from 2019 to 2022. In the CB [see Fig. 6(f)], the relations between surface deformation and hydraulic head undergone a transformation in 2018. That is, these two data sets change are relevant after 2018, which implies semiconfined and unconfined conditions in this basin. In addition, during 2018 to 2021, surface deformation and hydraulic heads characterize annual amplitudes of 4.3 ± 0.1 mm and 0.29 ± 0.1 m, respectively.

V. DISCUSSION

A. Historical Hydraulic Head Change in the SGV and CPOC

Our study reveals upward trends in hydraulic heads within the SGV and CPOC regions between Jun. 2015 and Nov. 2021. However, it is noteworthy that these two basins have been previously characterized by substantial groundwater depletion and the resulting land subsidence over the past few decades [5], [7], [8]. To thoroughly examine the dynamics of groundwater levels

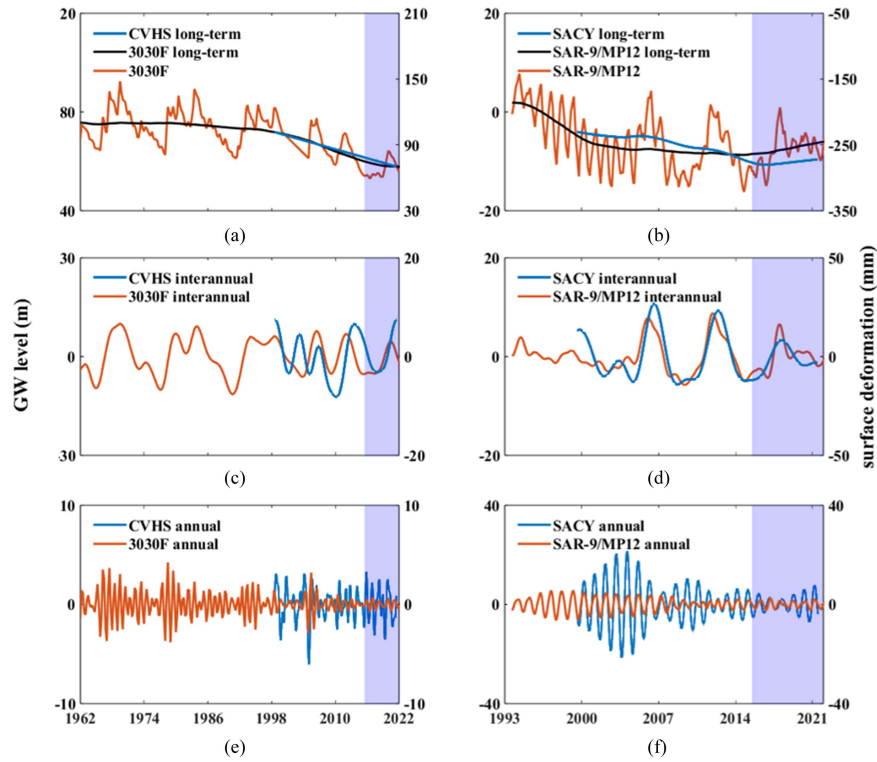


Fig. 7. Multitemporal characteristics of historical hydraulic heads and surface deformations at 3030F and GNSS station CVHS (a), (c), and (e), and SAR-9/MP12 and GNSS station SACY (b), (d), and (f).

and establish the preconsolidation head for assessing changes in IGWS and RGWS, we analyze the temporal variations in historical hydraulic heads at two representative wells and compare them with the multitemporal surface deformations observed at nearby GNSS stations.

At well 3030F (in the SGV), the hydraulic heads exhibited a continuous downward trend that commenced in 1964. This trend gained momentum from 1999 onwards and gradually moderated until 2019 [see Fig. 7(a)]. Meantime, a persistent decreasing pattern was noted in the deformation observed at the GNSS station CVHS. Besides, both GNSS and head datasets had significant 6.8-year interannual fluctuations starting from 2019 [see Fig. 7(c)]. Consequently, when assessing the trend of groundwater levels between 2015 and 2022, a positive rate is computed due to these dynamic changes. Besides, the results reveal an identical pattern between hydraulic head and precipitation with a correlation coefficient of 0.95 (Fig. S10), underlining that the interannual ground-water level change is largely modulated by precipitation.

At well MP12 and GNSS station SACY (in the CPOC), both hydraulic head and surface deformation exhibited sustained decreasing trends until 2015, after which they began to rise [see Fig. 7(b)]. The decomposed results further reveal a 6.5-year interannual change for GNSS and head datasets, reaching peaks in 2006, 2012, and 2018 [see Fig. 7(d)]. Besides, from 2015 to 2022, the interannual change caused gradual increase in these two data. This pattern suggests that the hydraulic head remained above the preconsolidation head during the entire study period. Additionally, the interannual hydraulic head variations notably displayed a reduced peak-to-peak amplitude between 2015 and

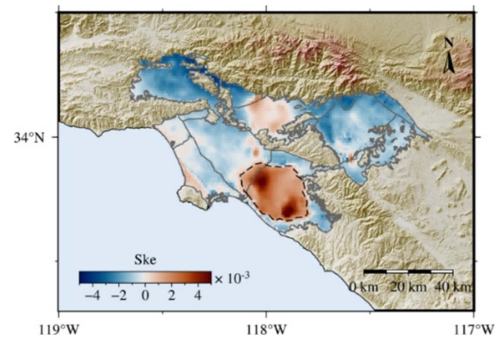


Fig. 8. Spatial distribution of elastic skeletal storativity across the study area. The “bowl” area is represented by the dotted line.

2020, with a sudden drop observed from 2018 to 2019. This indicates a shorter water cycle and a drier season. Moreover, these two data exhibited diminished annual fluctuations post-2008 [see Fig. 7(f)]. To account for these fluctuations, we introduced a multitemporal analysis of precipitation changes in the CPOC region (Fig. S11). The results further confirmed a declining trend in both annual and interannual precipitations, implying that the CPOC area has transitioned into a drier climatic phase.

B. GWS Changes in the CPOC

Having obtained the seasonal pixel-level changes in hydraulic head, we proceeded to estimate the elastic skeletal storativity across the entire study area using (3). As illustrated in Fig. 8, the values of range from -3.71×10^{-3} to 5.78×10^{-3} across the study area, which agrees well with findings from Riel et

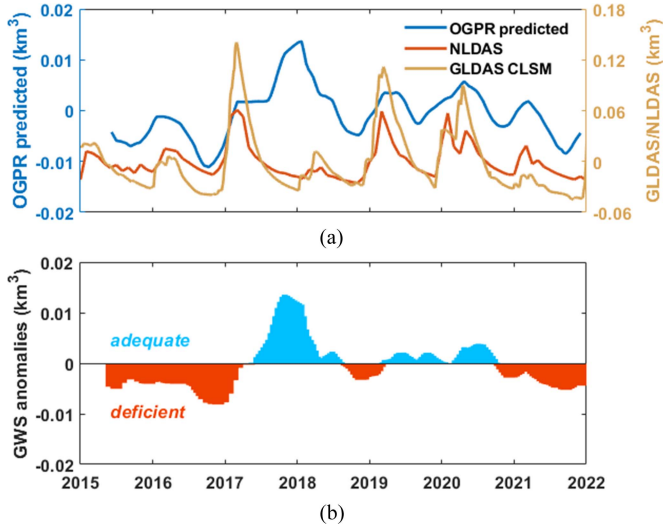


Fig. 9. (a) Comparison of ML-predicted seasonal GWS change and GLDAS CLSM and NLDAS model outputs. (b) Wet and dry year shown by the GWS anomalies.

al. [5]. The spatial distribution of corresponds to the amplitude map [see Fig. 5(b)], highlighting significant values in the CPOC regions. Our results recognize the most prominent in the “bowl” area, encompasses the majority of the CPOC and eastern margin of the CB. Here, the average value reaches up to 2.31×10^{-3} , indicating a robust storage capacity within the aquifer system in this region [5].

Based on the last sections, we could conclude that the CPOC experienced RGWS variation throughout the study period. Thus, with computed S_{ke} , our results reveal $(1.2 \pm 0.05) \times 10^6 \text{ m}^3$ annual fluctuations of the seasonal GWS change in the CPOC, ultimately leading to an accumulation of about $2.5 \times 10^6 \text{ m}^3$ of RGWS during 2015–2022.

C. Comparison of Modeled and Predicted Seasonal GWS Variations in the CPOC

In Section IV-B, we established that the ML-predicted groundwater levels exhibit stronger correlations with the observed hydraulic heads compared to model outputs. Here, we conduct a direct comparison between the predicted and mode outputs to underline the advantages of our method in obtaining seasonal GWS changes within coastal areas, specifically the CPOC. As shown in Fig. 9(a), predicted results manifest low relevance with model outputs by CC of 0.26 for GLDAS CLSM and 0.36 for NLDAS. Notably, a significant disagreement between these three datasets emerges in the year 2018, where the predicted results display significantly elevated GWS variations.

As stated in Section III-A, the seasonal hydraulic heads involve interannual variability, which provides crucial insights into the abnormal groundwater level change. Given the high consistency between the ML-predicted groundwater levels and observed data, we delve into investigating the multitemporal variability of hydraulic heads to elucidate the anomalous GWS change observed in 2018. As illustrated in Fig. S6b and d, both the annual and interannual signals concurrently peaked around

the winter of 2018, resulting in hydraulic heads that were at their highest throughout the study period.

We introduce precipitation from NLDAS to explore the climatological mechanisms behind the abnormal accumulation in 2018. Previous work has reported a wet season in 2017 across the entire study area [8], a pattern consistent with the NLDAS intensive precipitation (Fig. S11). Considering the relatively limited groundwater flow between basins [8], we speculate the extreme GWS change in 2018 is due to the intense precipitation in 2017. This circumstance indicates that a significant portion of the precipitation remained within the CPOC, ultimately infiltrating into the deep aquifers as groundwater recharges. Moreover, diverted rivers and streams contribute to replenishing the groundwater levels within the basin.

Compared to hydrological models, our ML-based method not only demonstrates enhanced efficacy in reconstructing GWS changes but also proves to be more adaptable in capturing extreme change events. Furthermore, by subtracting the mean annual GWS change, we obtained the GWS anomalies [see Fig. 9(b)]. The result obviously revealed distinctive patterns: GWS was adequate during mid-2017 to late 2018, yet deficient in 2015 to early 2017, and late 2020 to 2022.

D. Advantages and Limitations of This Study

Previous research used the spatial interpolation method, like Kriging interpolation and IDW interpolation, to the hydraulic head data to align with the spatial resolution of InSAR measurements. Even their results can reveal the main regions with significant long-term and seasonal hydraulic head changes similar to our research, such as the SGV and CPOC, but for places with very few observation wells, their results are not reliable. In addition, traditional interpolation methods have difficulties in considering geological settings and climate factors simultaneously during the interpolating process, which would bias the estimation of fine-scale aquifer parameters. In our study, integrating InSAR measurements and hydraulic head data using the ML approach would provide new insights for finer-scale groundwater level changes monitoring, regional groundwater management, and more accurate aquifer parameters estimation. Besides, this study offers another way for monitoring the fluctuations of groundwater level using the dv/v , which can provide cross-validation for the ML results.

However, due to the data span of InSAR measurement employed is short (Jun. 2015–Nov. 2021), it is challenging to study the spatiotemporal characteristics of ~ 6.5 -years water cycle utilizing InSAR data. In the future, we would extend our InSAR measurement jointly using the historic Envisat satellites images and the latest Sentinel 1A data (or NiSAR data). Additionally, in the future, we would add descending Sentinel 1A data and Sentinel 1B data to improve the accuracy of land deformation measurements and their temporal resolution.

VI. CONCLUSION

In this study, we investigated the spatiotemporal characteristics of InSAR deformations and groundwater levels from observation wells across Los Angeles and Orange County from Jun.

2015 to Nov. 2021. The results illustrate a substantial correlation between those two datasets. By applying the blind source separation, we found that the inelastic surface deformation induced by the long-term hydraulic head changes mainly happened in the SGV. In contrast, the seasonal deformation is primarily concentrated in the CPOC.

Continuing our investigation into GWS changes and aquifer characteristics, we proceeded to train the OGPR model. This model was specifically employed to directly predict both the long-term and seasonal hydraulic head changes at InSAR pixel scale across the entire study region. The results revealed a mean increase of 0.28 ± 0.05 m/yr for long-term groundwater levels during the study period, which is related to the ascending phase of multiyear groundwater level changes, such as the 6.5-year water cycle in the SGV and CPOC.

The pronounced variations in seasonal groundwater level changes are particularly prominent in the SGV and CPOC, which is found to be correlated with heavy winter precipitation. Further in comparison with both dv/v measurements and outputs from hydrological models, our proposed ML-based methodology emerges as highly promising for accurately capturing both long-term and seasonal groundwater level changes, while also effectively documenting instances of extreme events. As new satellites continue to be launched and mass data freely available, we believe that the InSAR technique will progressively assume a more crucial role in groundwater monitoring, especially when integrated with other geodetic data sources. We anticipate that this study will serve as a valuable reference point, contributing to the advancement of methodologies for ground-water monitoring and fostering enhanced understanding of hydrological dynamics.

ACKNOWLEDGMENT

The Sentinel-1A images are freely available on the Alaska Satellite Facility-Distributed Active Archive Center (<https://search.asf.alaska.edu/>); The NLDAS (<https://ldas.gsfc.nasa.gov/nldas>) and GLDAS CLSM data (<https://ldas.gsfc.nasa.gov/gldas>) can both be obtained from NASA; The GNSS VDTs are provided by the Nevada Geodetic Laboratory (<http://geodesy.unr.edu/>); The atmospheric correction data is downloaded from Generic Atmospheric Correction Online Service for InSAR (GACOS).

REFERENCES

- [1] M. Béjar-Pizarro et al., "Mapping groundwater level and aquifer storage variations from InSAR measurements in the Madrid aquifer, Central Spain," *J. Hydrol.*, vol. 547, pp. 678–689, Apr. 2017.
- [2] E. Chaussard, P. Milillo, R. Bürgmann, D. Perissin, E. J. Fielding, and B. Baker, "Remote sensing of ground deformation for monitoring groundwater management practices: Application to the Santa Clara Valley during the 2012–2015 California drought," *J. Geophys. Res. Solid Earth*, vol. 122, no. 10, pp. 8566–8582, 2017.
- [3] F. Cigna and D. Tapete, "Land subsidence and aquifer-system storage loss in Central Mexico: A quasi-continental investigation with Sentinel-1 InSAR," *Geophys. Res. Lett.*, vol. 49, no. 15, 2022, Art. no. e2022GL098923.
- [4] L. Jiang, L. Bai, Y. Zhao, G. Cao, H. Wang, and Q. Sun, "Combining InSAR and hydraulic head measurements to estimate aquifer parameters and storage variations of confined aquifer system in Cangzhou, North China Plain," *Water Resour. Res.*, vol. 54, no. 10, pp. 8234–8252, 2018.
- [5] B. Riel, M. Simons, D. Ponti, P. Agram, and R. Jolivet, "Quantifying ground deformation in the Los Angeles and Santa Ana Coastal Basins due to groundwater withdrawal," *Water Resour. Res.*, vol. 54, no. 5, pp. 3557–3582, 2018.
- [6] W. R. Neely, A. A. Borsa, J. A. Burney, M. C. Levy, F. Silverii, and M. Sneed, "Characterization of groundwater recharge and flow in California's San Joaquin Valley from InSAR-observed surface deformation," *Water Resour. Res.*, vol. 57, no. 4, 2021, Art. no. e2020WR028451.
- [7] T. Clements and M. A. Denolle, "Tracking groundwater levels using the ambient seismic field," *Geophys. Res. Lett.*, vol. 45, no. 13, pp. 6459–6465, 2018.
- [8] S. Mao, A. Lecointre, R. D. van der Hilst, and M. Campillo, "Space-time monitoring of groundwater fluctuations with passive seismic interferometry," *Nat. Commun.*, vol. 13, no. 1, Aug. 2022, Art. no. 4643.
- [9] J. Chen, J. Li, Z. Zhang, and S. Ni, "Long-term groundwater variations in Northwest India from satellite gravity measurements," *Glob. Planet. Change*, vol. 116, pp. 130–138, May 2014.
- [10] B. Li et al., "Global GRACE data assimilation for groundwater and drought monitoring: Advances and challenges," *Water Resour. Res.*, vol. 55, no. 9, pp. 7564–7586, 2019.
- [11] B. R. Scanlon et al., "Groundwater depletion and sustainability of irrigation in the US high plains and Central Valley," *Proc. Nat. Acad. Sci.*, vol. 109, no. 24, pp. 9320–9325, Jun. 2012.
- [12] M. Rodell, J. Chen, H. Kato, J. S. Famiglietti, J. Nigro, and C. R. Wilson, "Estimating groundwater storage changes in the Mississippi River basin (USA) using GRACE," *Hydrogeology J.*, vol. 15, no. 1, pp. 159–166, Feb. 2007.
- [13] B. R. Scanlon et al., "Global models underestimate large decadal declining and rising water storage trends relative to GRACE satellite data," *Proc. Nat. Acad. Sci.*, vol. 115, no. 6, pp. E1080–E1089, Feb. 2018.
- [14] K. H. Ji and T. A. Herring, "Correlation between changes in groundwater levels and surface deformation from GPS measurements in the San Gabriel Valley, California," *Geophys. Res. Lett.*, vol. 39, no. 1, 2012.
- [15] N. E. King et al., "Space geodetic observation of expansion of the San Gabriel Valley, California, aquifer system, during heavy rainfall in winter 2004–2005," *J. Geophysical Res. B, Solid Earth*, vol. 112, no. B3, 2007.
- [16] K. Zhu, X. Zhang, Q. Sun, H. Wang, and J. Hu, "Characterizing spatiotemporal patterns of land deformation in the Santa Ana Basin, Los Angeles, from InSAR Time Series and Independent Component Analysis," *Remote Sens.*, vol. 14, no. 11, Jan. 2022, Art. no. 2624.
- [17] K. M. Watson, Y. Bock, and D. T. Sandwell, "Satellite interferometric observations of displacements associated with seasonal groundwater in the Los Angeles basin," *J. Geophys. Res. Solid Earth*, vol. 107, no. B4, pp. ETG–ET8, 2002.
- [18] H. Adun et al., "Estimation of thermophysical property of hybrid nanofluids for solar thermal applications: Implementation of novel optimizable Gaussian Process regression (O-GPR) approach for viscosity prediction," *Neural Comput. Appl.*, vol. 34, no. 13, pp. 11233–11254, Jul. 2022.
- [19] N. Berg et al., "Twenty-first-century precipitation changes over the Los Angeles region," *J. Climate*, vol. 28, no. 2, pp. 401–421, Jan. 2015.
- [20] E. Chaussard, R. Bürgmann, M. Shirzaei, E. J. Fielding, and B. Baker, "Predictability of hydraulic head changes and characterization of aquifer-system and fault properties from InSAR-derived ground deformation," *J. Geophys. Res. Solid Earth*, vol. 119, no. 8, pp. 6572–6590, 2014.
- [21] D. P. S. Bekaert, A. Hooper, and T. J. Wright, "A spatially variable power law tropospheric correction technique for InSAR data," *J. Geophys. Res. Solid Earth*, vol. 120, no. 2, pp. 1345–1356, 2015.
- [22] K. D. Murray, R. B. Lohman, and D. P. S. Bekaert, "Cluster-based empirical tropospheric corrections applied to InSAR time series analysis," *IEEE Trans. Geosci. Remote Sens.*, vol. 59, no. 3, pp. 2204–2212, Mar. 2021.
- [23] C. Yu, Z. Li, N. T. Penna, and P. Crippa, "Generic atmospheric correction model for interferometric synthetic aperture radar observations," *J. Geophys. Res. Solid Earth*, vol. 123, no. 10, pp. 9202–9222, 2018.
- [24] W. R. Neely, A. A. Borsa, and F. Silverii, "GInSAR: A cGPS correction for enhanced InSAR time series," *IEEE Trans. Geosci. Remote Sens.*, vol. 58, no. 1, pp. 136–146, Jan. 2020.
- [25] D. Clarke, L. Zaccarelli, N. M. Shapiro, and F. Brenguier, "Assessment of resolution and accuracy of the moving window cross spectral technique for monitoring crustal temporal variations using ambient seismic noise," *Geophys. J. Int.*, vol. 186, no. 2, pp. 867–882, Aug. 2011.
- [26] T. Lecocq, L. Longuevergne, H. A. Pedersen, F. Brenguier, and K. Stammler, "Monitoring ground water storage at mesoscale using seismic noise: 30 years of continuous observation and thermo-elastic and hydrological modeling," *Sci. Rep.*, vol. 7, no. 1, Oct. 2017, Art. no. 14241.

- [27] M. Rodell et al., "The global land data assimilation system," *Bull. Amer. Meteorological Soc.*, vol. 85, pp. 381–394, Mar. 2004.
- [28] H. Wei, Y. Xia, K. E. Mitchell, and M. B. Ek, "Improvement of the Noah land surface model for warm season processes: Evaluation of water and energy flux simulation," *Hydrol. Process.*, vol. 27, no. 2, pp. 297–303, 2013.
- [29] A. Hyvärinen and E. Oja, "Independent component analysis: Algorithms and applications," *Neural Netw.*, vol. 13, no. 4, pp. 411–430, Jun. 2000.
- [30] Z. Jiang, Y.-J. Hsu, L. Yuan, and D. Huang, "Monitoring time-varying terrestrial water storage changes using daily GNSS measurements in Yunnan, Southwest China," *Remote Sens. Environ.*, vol. 254, Mar. 2021, Art. no. 112249.
- [31] S. K. Ebmeier, "Application of independent component analysis to multi-temporal InSAR data with volcanic case studies," *J. Geophys. Res. Solid Earth*, vol. 121, no. 12, pp. 8970–8986, 2016.
- [32] K. Dragomiretskiy and D. Zosso, "Variational mode decomposition," *IEEE Trans. Signal Process.*, vol. 62, no. 3, pp. 531–544, Feb. 2014.
- [33] N. E. Huang and Z. Wu, "A review on Hilbert-Huang transform: Method and its applications to geophysical studies," *Rev. Geophys.*, vol. 46, no. 2, 2008.
- [34] G. Alkhayat and R. Mehmood, "A review and taxonomy of wind and solar energy forecasting methods based on deep learning," *Energy AI*, vol. 4, Jun. 2021, Art. no. 100060.
- [35] S. Wu et al., "Multitemporal mass change analysis of Greenland Ice Sheet using variational mode decomposition," *Geophys. J. Int.*, vol. 230, no. 3, pp. 1711–1724, Sep. 2022.
- [36] J. Chen, R. Knight, H. A. Zebker, and W. A. Schreüder, "Confined aquifer head measurements and storage properties in the San Luis Valley, Colorado, from spaceborne InSAR observations," *Water Resour. Res.*, vol. 52, no. 5, pp. 3623–3636, 2016.
- [37] B. Chen et al., "Land subsidence and its relation with groundwater aquifers in Beijing Plain of China," *Sci. Total Environ.*, vol. 735, Sep. 2020, Art. no. 139111.
- [38] S. Majumdar, R. Smith, J. J. Butler Jr., and V. Lakshmi, "Groundwater withdrawal prediction using integrated multitemporal remote sensing data sets and machine learning," *Water Resour. Res.*, vol. 56, no. 11, 2020, Art. no. e2020WR028059.
- [39] R. G. Smith et al., "Mapping groundwater use with satellite sensor fusion and machine learning," *Geological society of america abstracts with programs*, vol. 53, no. 6, Oct. 2021.
- [40] R. G. Smith and S. Majumdar, "Groundwater storage loss associated with land subsidence in Western United States mapped using machine learning," *Water Resour. Res.*, vol. 56, no. 7, 2020, Art. no. e2019WR026621.
- [41] H. Tao et al., "Groundwater level prediction using machine learning models: A comprehensive review," *Neurocomputing*, vol. 489, pp. 271–308, Jun. 2022.
- [42] H. Wang, C. Jia, P. Ding, K. Feng, X. Yang, and X. Zhu, "Analysis and prediction of regional land subsidence with InSAR technology and machine learning algorithm," *KSCE J. Civil Eng.*, vol. 27, no. 2, pp. 782–793, Feb. 2023.
- [43] S. A. Naghibi, B. Khodaei, and H. Hashemi, "An integrated InSAR-machine learning approach for ground deformation rate modeling in arid areas," *J. Hydrol.*, vol. 608, May 2022, Art. no. 127627.
- [44] G. Wang, P. Li, Z. Li, J. Liu, Y. Zhang, and H. Wang, "InSAR and machine learning reveal new understanding of coastal subsidence risk in the Yellow River Delta, China," *Sci. Total Environ.*, vol. 915, Mar. 2024, Art. no. 170203.
- [45] R. Shamshiri, M. Motagh, H. Nahavandchi, M. H. Haghighi, and M. Hoseini, "Improving tropospheric corrections on large-scale Sentinel-1 interferograms using a machine learning approach for integration with GNSS-derived zenith total delay (ZTD)," *Remote Sens. Environ.*, vol. 239, Mar. 2020, Art. no. 111608.
- [46] A. Bayati, K.-K. Nguyen, and M. Cheriet, "Gaussian process regression ensemble model for network traffic prediction," *IEEE Access*, vol. 8, pp. 176540–176554, 2020.
- [47] C. Lin, T. Li, S. Chen, X. Liu, C. Lin, and S. Liang, "Gaussian process regression-based forecasting model of dam deformation," *Neural Comput. Appl.*, vol. 31, no. 12, pp. 8503–8518, Dec. 2019.
- [48] R. G. Smith et al., "Estimating the permanent loss of groundwater storage in the Southern San Joaquin Valley, California," *Water Resour. Res.*, vol. 53, no. 3, pp. 2133–2148, 2017.
- [49] L. Zhang, Z. Lu, X. Ding, H. Jung, G. Feng, and C.-W. Lee, "Mapping ground surface deformation using temporarily coherent point SAR interferometry: Application to Los Angeles Basin," *Remote Sens. Environ.*, vol. 117, pp. 429–439, Feb. 2012.
- [50] L. Bai et al., "Quantifying the influence of long-term overexploitation on deep groundwater resources across Cangzhou in the North China Plain using InSAR measurements," *J. Hydrol.*, vol. 605, Feb. 2022, Art. no. 127368.
- [51] M. M. Miller and M. Shirzaei, "Spatiotemporal characterization of land subsidence and uplift in Phoenix using InSAR time series and wavelet transforms," *J. Geophys. Res. Solid Earth*, vol. 120, no. 8, pp. 5822–5842, 2015.
- [52] M. M. Miller, M. Shirzaei, and D. Argus, "Aquifer mechanical properties and decelerated compaction in Tucson, Arizona," *J. Geophys. Res. Solid Earth*, vol. 122, no. 10, pp. 8402–8416, 2017.



Shuaiying Wu received the B.S. degree in surveying and mapping engineering from the East China University of Technology, Fuzhou, China, in 2009, and the M.S. degree in photogrammetry and remote sensing in 2012 from Southwest Jiaotong University, Chengdu, China, where she is currently working toward the Ph.D. degree in photogrammetry and remote sensing with the Faculty of Geosciences and Environmental Engineering.

She is mainly involved in groundwater monitoring combined with various remote-sensing methods InSAR, GRACE, and GPS. Her current research interests include groundwater monitoring combined with various remote sensing methods, InSAR, GRACE, and GNSS.



Guoxiang Liu received the B.Eng. degree in surveying engineering from the East China Institute of Geology, Jiangxi, China, in 1991, the M.Eng. degree in geomatics from the Southwest Jiaotong University, Chengdu, China, in 1994, and the Ph.D. degree in remote sensing from The Hong Kong Polytechnic University, Hong Kong, in 2003.

He is currently a Professor with the Department of Remote Sensing and Geospatial Information Engineering, Southwest Jiaotong University. From Sep. 2005 to Sep. 2006, he was a Visiting Scholar and

conducted research on InSAR with Dr. S. M. Buckley with the Department of Aerospace Engineering and Engineering Mechanics, The University of Texas at Austin, TX, USA. He has authored three books, more than 170 articles and holds twelve patents. His current research interests include InSAR, PSI, radar interferometry and digital photogrammetry for regional mapping topography, and deformation. Dr. Liu was a Co-Chair of the Working Group VII of the ISPRS Technical Commission VII and a Member of the Commission on Mapping from Satellite Imagery of the International Cartographic Association.



Xiaowen Wang (Member, IEEE) received the B.S. degree in geomatics from Henan Polytechnic University, Jiaozuo, China, in 2010, and the Ph.D. degree in photogrammetry and remote sensing from Southwest Jiaotong University, Chengdu, China, in 2017.

Between Sep. 2017 and Mar. 2019, he was a Postdoctoral Researcher with the Tokyo University, Japan. Between Sep. 2021 and Aug. 2022, he was a Research Scientist with the Dublin University, Ireland. He is currently an Associate Professor with the Faculty of Geosciences and Environmental Engineering, South-

west Jiaotong University, Chengdu, China, where he is mainly involved in crustal deformation measuring and modeling studies with remote sensing techniques, such as InSAR, sub-pixel image cross-correlation, and digital elevation model differencing.



Hongguo Jia received the bachelor's degree in planning and management of resource and environment from Wuhan University, Wuhan, China, the master's degree in surveying from the University of Applied Sciences in Stuttgart, Stuttgart, Germany, and the Ph.D. degree in remote sensing from the Southwest Jiaotong University, Chengdu, China.

She is currently an Associate Professor with the Faculty of Geosciences and Engineering, Southwest Jiaotong University. Her research interests include advanced processing developments for multitemporal

SAR interferometry and deformation monitoring.



Bo Zhang received the B.Eng., M.Eng., and Ph.D. degrees in photogrammetry and remote sensing from the Southwest Jiaotong University, Chengdu, China, in 2010, 2014, and 2022, respectively.

He is currently a Postdoctoral Fellow and an Assistant Research Fellow with the Institute of Mountain Hazards and Environment, Chinese Academy of Sciences, Chengdu, China. His research interests include glaciology remote sensing, disaster remote sensing, time-series interferometric synthetic aperture radar, and unmanned aerial vehicle photogrammetry.



Yihang Ding received the B.Eng. degree in surveying engineering from Wuhan University, Wuhan, China, in 2015, the M.Eng. degree in surveying engineering from Southwest Jiaotong University, Chengdu, China, in 2018, and the Ph.D. degree in geodetic science from the Ohio State University, Columbus, OH, USA, in 2023.

He is currently a Postdoctoral with the Department of Hydraulic Engineering, Tsinghua University, Beijing, China. His current research interests include hydrological geodesy based on GNSS, GRACE, Satellite

Altimetry, and InSAR.



Wenfei Mao (Member, IEEE) received the B.S. and M.S. degrees in surveying engineering from East China University of Technology, Fuzhou and Nanchang, China, in 2013 and 2018, respectively, and the Ph.D. degree in photogrammetry and remote sensing from Southwest Jiaotong University, Chengdu, China, in 2022.

Between Oct. 2022 and Jul. 2024, he was a Postdoctoral Fellow with the Institute of Space and Earth Information Science of the Chinese University of Hong Kong, Hong Kong. He is currently an Assistant

Professor with the Faculty of Geosciences and Engineering, Southwest Jiaotong University, Chengdu, China. His current research interests include coupling relationship between ionospheric anomalies and earthquakes, ionospheric modeling and correcting for InSAR, SAR/InSAR-based ionospheric TEC mapping, InSAR-based, and geological hazard monitoring.